Accurate cross-sectional stress profiling of optical fibers

Michael R. Hutsel,* Reeve Ingle, and Thomas K. Gaylord

School of Electrical and Computer Engineering, Georgia Institute of Technology, 777 Atlantic Drive, N.W., Atlanta, Georgia 30332-0250, USA

*Corresponding author: tgaylord@ece.gatech.edu

Received 16 July 2009; revised 21 August 2009; accepted 23 August 2009; posted 24 August 2009 (Doc. ID 114374); published 2 September 2009

A novel technique for determining two-dimensional, cross-sectional stress distributions in optical fibers and fiber-based devices is presented. Use of the Brace–Köhler compensator technique and a polarization microscope for the measurement of retardation due to stress-induced birefringence is described, along with the tomographic reconstruction process for the determination of stress. Measurements are performed on Corning SMF-28 fiber in an unperturbed section, a section near a cleaved end-face, and a section exposed to CO_2 laser radiation. Cross-sectional stress distributions are presented. Stress relaxation is quantified in the cleaved fiber and the fiber exposed to CO_2 laser radiation.

OCIS codes: 060.2270, 060.2400, 110.0180, 120.5410.

1. Introduction

As optical fiber and fiber-based devices continue to expand beyond a waveguiding role, there is an increasing need to understand their fundamental physical characteristics. Stresses induced in optical fibers during manufacturing, both by differences in coefficient of thermal expansion and differences in viscosity, are known to affect the refractive index of the fiber [1,2]. Stress induced by differences in coefficient of thermal expansion is typically referred to as thermally induced stress. Stress induced by differences in viscosity is typically referred to as draw-induced or mechanically induced stress. Both of these stresses, referred to as frozen-in or residual stresses, remain in the optical fiber after manufacture without the presence of externally applied forces [3]. Both the presence and modification of frozen-in stress (1) inherently affects existing fibers and devices and (2) enables novel devices and applications. The presence of frozen-in stress is detrimental to applications where polarization insensitivity is required, such as tunable filters for wavelength-division-multiplexed systems [4]. However, frozen-in stress is required in other applications. Stress-inducing regions are necessary to create the high birefringence necessary in certain types of polarization-maintaining fiber [5].

Modification of frozen-in stress due to fiber preparation techniques such as cleaving can result in unexpected changes in fiber characteristics [6]. However, changes in frozen-in stress due to fiber modification techniques enable the fabrication of fiber-based devices such as fiber Bragg gratings and long-period fiber gratings (LPFGs). A variety of techniques enable the controlled modification of frozen-in stress, including exposure of the fiber to ultraviolet laser radiation [7], carbon dioxide (CO_2) laser radiation [8–12], femtosecond laser radiation [13], and electric arc discharge [14]. With the increasing need for and the vast number of applications of specialty fiber and fiber-based devices, accurate knowledge of the stress present in optical fibers is critical for design, manufacturing, and characterization.

Birefringence induced by frozen-in stress can be exploited to determine nondestructively the stress present in optical fibers. The polarization retardation of light propagating normal to the fiber axis can be determined using photoelastic measurement

0003-6935/09/264985-11$15.00/0

techniques. From measurements of the magnitude of retardation, the axial stress in the fiber can be evaluated. In a fiber with an azimuthally symmetric axial stress distribution, a single radial profile fully characterizes the stress. In this case, the axial stress profile can be calculated from the inverse Abel transform of a retardation measurement [15–20]. For fibers with azimuthally asymmetric axial stress distributions, a full cross-sectional distribution is required to characterize the stress. Computed tomography techniques enable the determination of the full cross-sectional axial stress distribution from a sequence of retardation measurements taken over multiple rotational angles of the fiber [21–25]. For both symmetric and asymmetric fibers, the retardation measurement from which the stress is evaluated must be suitably accurate.

Several techniques exist for measuring the retardation produced by the birefringence in optical fibers. Polarization digital holographic microscopy enables the determination of retardation from a single intensity pattern produced by the interference of two reference beams and a beam passing through the optical fiber [26]. This technique, however, requires several beam-splitting prisms, wave plates, and polarizers to control the directions and polarizations of the three beams of light. Phase-stepping photoelasticity enables the determination of the retardation from several intensity patterns recorded for predetermined orientations of wave plates and polarizers in the beam path [19,25]. This technique requires only one beam path but can require multiple wave plates to generate a sufficient number of intensity patterns. Furthermore, this techniques relies on the measurement of relative intensities, which in general is not as accurate as detecting a minimum or null of intensity. Phase modulation techniques enable the determination of the retardation from several intensity patterns recorded as the orientation of a known phase modulator is changed sequentially [27]. As with phase-stepping photoelasticity, phase modulation techniques rely on the measurement of relative intensities. Furthermore, phase modulation techniques require the use of a custom phase modulator, rather than commercially available wave plates.

To avoid the need to measure relative intensities, phase compensation techniques are often used to measure the retardation produced by optical fibers. Current techniques build upon the use of a polariscope and the Sénarmont compensation technique introduced by Chu and Whitbread [15]. The polariscope requires a single beam path, a wave plate, and two polarizers. The measurement technique involves the rotation of a polarizer placed in the beam path after the fiber sample (commonly referred to as the analyzer) until a minimum in transmitted intensity is found. From the analyzer angle that produces the minimum of intensity, the retardation imparted by the fiber can be determined. Several improvements to this technique have been made to increase the accuracy of the polariscope. The addition of a diffuser following the He–Ne laser light source by Raine *et al.* eliminates interference effects due to diffraction of the coherent source [16]. Park *et al.* enabled higher accuracy with a high-magnification imaging system by rearranging the optical components [17,18]. Previous arrangements of the polariscope placed the fixed polarizer before the fiber sample and a quarter-wave plate (QWP) and rotating polarizer (analyzer) after the fiber. With the introduction of high-magnification imaging of the fiber, wavefront distortions after the imaging system reduce the spatial uniformity of the retardation imparted by the QWP [17]. By reversing the placement of the polariscope components, placing the rotating polarizer and QWP before the fiber sample and the fixed polarizer after, the wavefront quality upon the QWP is improved.

In spite of improvements to the polariscope configuration, it was recently shown that the Sénarmont compensation technique is generally not suitable to measure the low retardation produced by the small levels of birefringence found in typical optical fibers [28,29]. Measurements of silica-based fiber indicate retardations of the order of a few nanometers for source wavelengths of 632.8 632.8 nm [15,17,24] and 546 nm [20,29]. For comparison, in a study of several compensation techniques by Montarou *et al.* [29], the average Sénarmont measurement error for retardations of 3.09 and 1.04 nm is 34.6% and 48.1%, respectively, for a source wavelength of 632.8 nm. Higher retardation measurement accuracies are needed to characterize the frozen-in stress present in telecommunications-grade fibers and fiber-based devices.

In this paper, we present a cross-sectional profiling technique to characterize accurately the frozen-in stress in fibers and fiber-based devices with small levels of birefringence. The Brace–Köhler compensation technique and a commercial polarization microscope yield high-accuracy retardation measurements. The use of a commercial polarization microscope avoids the need for a custom optical configuration and enables high-quality illumination from an incoherent source, eliminating interference effects due to diffraction of a coherent source. The Brace–Köhler compensation technique is used to measure accurately the small retardations produced by optical fibers. While both the Brace–Köhler and two-wave plate compensator techniques have been shown to measure accurately low levels of retardation [29], the Brace–Köhler technique is chosen due to the long measurement times required to characterize the full cross-sectional axial stress distribution using the two-wave plate compensator technique. From the retardation measurements, computed tomography principles enable the determination of the cross-sectional axial stress distributions.

The theories for compensator-based retardation measurement and stress profile determination using computed tomography are presented in Section 2.

The experimental measurement apparatus and data analysis techniques are described in Section 3. Stress distributions in Corning SMF-28 fiber in an unperturbed section, a section near a cleaved end face, and a section exposed to CO_2 laser radiation are presented in Section 4. Also presented in Section 4 are analyses of the axial variations in the mean stress in the cleaved fiber and the fiber exposed to CO_2 laser radiation. Section 4 is concluded with an assessment of the performance of the technique, and the results are summarized in Section 5.

2. Theory

Stress-induced birefringence in optical fibers and fiber-based devices enables nondestructive determination of the frozen-in stress present in the fiber. In the absence of external forces, the stress-optic law describes the relationship between the frozen-in stress and the resulting birefringence induced in the fiber. In general, the frozen-in stress, σ, can be decomposed into normal stress components, σ_x, σ_y, and σ_z, along three principal orthogonal directions indicated in Fig. 1. The stress induces changes in the isotropic index of the fiber material, n_0, giving rise to unique principal indices of refraction, n_x, n_y, and n_z. The anisotropic principal indices of refraction are related to the isotropic index by

$$\begin{aligned} n_x &= n_0 + C_1\sigma_x + C_2(\sigma_y + \sigma_z), \\ n_y &= n_0 + C_1\sigma_y + C_2(\sigma_x + \sigma_z), \\ n_z &= n_0 + C_1\sigma_z + C_2(\sigma_x + \sigma_y), \end{aligned} \tag{1}$$

where C_1 and C_2 are the stress-optic coefficients of the extraordinary wave and the ordinary wave, respectively. Solving for the difference between any two principal indices of refraction, in this case n_z and n_x, yields the stress-optic law

$$n_z - n_x = C(\sigma_z - \sigma_x), \tag{2}$$

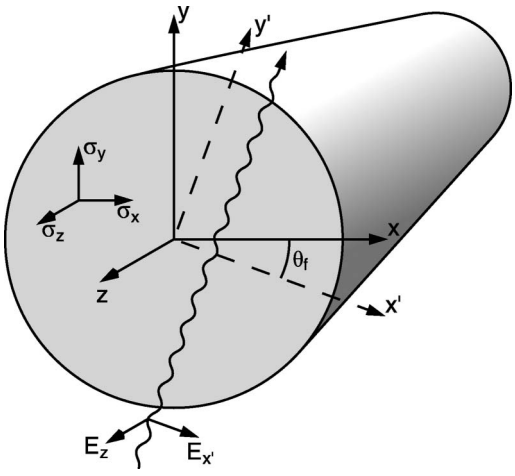

Fig. 1. Configuration of fiber illumination for birefringence measurements.

where $C = C_1 - C_2$ is commonly referred to as the stress-optic coefficient, or photoelastic constant.

Light which propagates normal to the fiber axis, z, and is linearly polarized at 45° relative to the fiber axis will result in equal polarizations in the axial and transverse directions. Illumination in this manner is illustrated in Fig. 1. Birefringence between the axial and the transverse indices of refraction will result in a path difference, or retardation between the axial and the transverse polarizations. By inspection of Fig. 1 and application of the stress-optic law, the retardation of a beam passing at an angle θ_f through the fiber can be written as

$$R(x', \theta_f) = \int_{-\infty}^{\infty} C[\sigma_z(x', y') - \sigma_{x'}(x', y')]\mathrm{d}y'. \tag{3}$$

In the absence of external forces, there is zero net stress on the $y'z$ plane of the optical fiber. This requires that the line integral of $\sigma_{x'}(x', y')$ in the y' direction be zero [30]. Thus, Eq. (3) simplifies to

$$R(x', \theta_f) = \int_{-\infty}^{\infty} C\sigma_z(x', y')\mathrm{d}y'. \tag{4}$$

Equation (4) relates the retardation of a beam passing at an angle θ_f through the fiber to the axial stress present in the fiber.

For an azimuthally symmetric fiber, the retardation profile is independent of θ_f, and the axial stress profile is determined from the inverse Abel transform of a single retardation profile [15]. For azimuthally asymmetric fibers, computed tomography principles enable the determination of the cross-sectional axial stress from a sequence of retardation profiles obtained over 180° of rotation of the optical fiber.

For each rotation angle of the fiber, θ_f, the Fourier slice theorem states that the one-dimensional Fourier transform of the retardation profile, $\tilde{R}$, is equal to a radial slice of the two-dimensional Fourier transform of the axial stress distribution, $C\tilde{\sigma}_z$. Defining s as the spatial angular frequency, this theorem is expressed as

$$\tilde{R}(s, \theta_f) = C\tilde{\sigma}_z(s\ \cos\theta_f, s\ \sin\theta_f), \tag{5}$$

where the coordinates $(s\ \cos\theta_f, s\ \cos\theta_f)$ define a slice at angle θ_f through the spatial angular frequency domain.

With retardation profiles spanning $0 \le \theta_f < 180°$, the entire cross-sectional stress distribution can be determined using this theorem. However, direct implementation of Eq. (5) requires the radial retardation profiles obtained in polar coordinates to be mapped to rectangular coordinates. This requires interpolation in the spatial angular frequency domain. Interpolation of spatial angular frequencies will affect all points in the real spatial domain, leading to interpolation errors across the entire stress distribution. To avoid frequency-domain interpolation,

filtered backprojection can be used to implement the Fourier slice theorem [31].

Expressing the inverse two-dimensional Fourier transform of Eq. (5) in the slice variables (s,θ_f), and recognizing that retardation profiles taken 180° apart are mirror images, the axial stress distribution can be expressed as

$$C\sigma_z(x\prime,y\prime)=\int_0^{\pi}\left[\int_{-\infty}^{\infty}\tilde{R}(s,\theta_f)|s|e^{i2\pi sx'}\mathrm{d}s\right]\mathrm{d}\theta. \qquad (6)$$

The quantity $\tilde{R}(s,\theta_f)|s|$ is the Fourier transform of an original retardation profile multiplied by a ramp in the spatial angular frequency domain. The ramp serves to filter the original retardation profile in reconstructing the stress distribution. In practice, however, the ramp filter may be modified for better performance with noisy data. Equation (6) is a form of the inverse Radon transform and allows the determination of the cross-sectional stress distribution from retardation measurements.

3. Methods

A. Brace–Köhler Compensator

A polarization microscope and the Brace–Köhler, or elliptical, compensation technique are used to measure the retardation induced by the birefringence in the fiber. A diagram of the relevant optical components is shown in Fig. 2.

A retardation measurement consists of first placing the fiber sample at 45° from extinction between crossed polarizers: the polarizer and analyzer in Fig. 2. Next, the compensator is inserted into the optical path at extinction and rotated until a minimum of intensity is observed following the analyzer. The magnitude of the retardation induced by the fiber sample, R_s, can then be determined by

$$R_s=|R_c\ \sin 2\theta_c|, \qquad (7)$$

where R_c is the retardation induced by the compensator and θ_c is the rotation of the compensator from extinction. The use of Eq. (7) requires the retardation induced by the fiber sample to be less than the retardation induced by the compensator. This is satisfied for the measurement of optical fibers. The relatively low levels of birefringence found in optical fibers induce much smaller retardations than the available compensators.

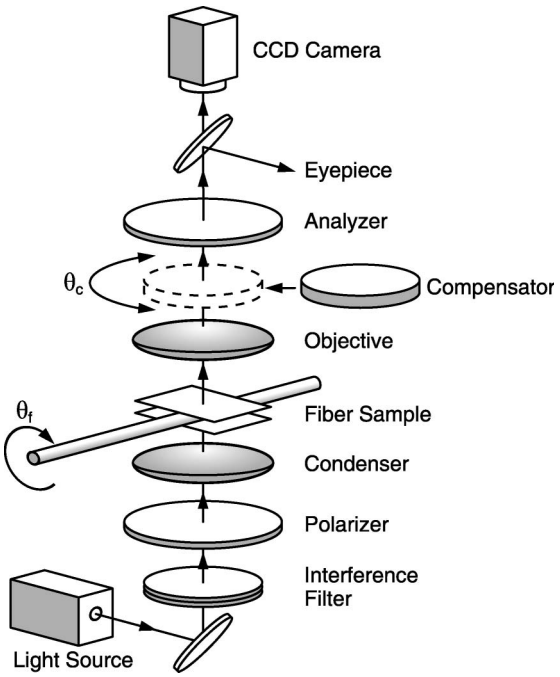

Fig. 2. Arrangement of the polarization microscope optical components and a fiber sample used for full-field retardation measurements. Rotation of the compensator during a full-field measurement is indicated by θ_c. Axial rotation of the fiber between full-field measurements is indicated by θ_f.

B. Full-Field Retardation Measurement

The spatially varying birefringence in optical fibers induces a nonuniform retardation over the field of view of the microscope. Thus, the compensator angle which produces a minimum of intensity after the analyzer will vary for each resolvable spot within the field of view. The polarization microscope and use of a full-field measurement technique similar to that used with the two-wave plate compensator [29] enables the rapid determination of the retardation over the entire field of view. The full-field measurement technique consists of acquiring images of the field of view for various compensator angles, θ_c. A range of compensator angles, θ_1 to θ_N, is chosen such that for $\theta_1 \le \theta_c < \theta_N$, a minimum of intensity is observed for every resolvable spot, or pixel, of the captured image. The compensator is rotated sequentially from θ_1 to θ_N in small increments, typically 0.5°, and an image is captured at each increment and stored for later processing. The dashed enclosed portion of the flow chart in Fig. 3 represents the full-field measurement.

For a single full-field measurement, processing consists of analyzing for each pixel the variation in intensity with changing compensator angle. The variation in intensity with changing compensator angle is fit with an nth order polynomial. The order of the polynomial is chosen based on qualitative assessment of the polynomial fit and standard deviation between the fit and the experimental data. Typically, a 5th or 6th order polynomial is used. The compensator angle producing minimum intensity is then found from the minimum of the polynomial. Equation (7) allows the calculation of the retardation for each pixel over the entire field of view. In addition to performing a full-field measurement on the fiber, a full-field measurement is also performed without the fiber. This measurement allows for subtraction of background retardation induced by birefringence in the optical components of the microscope.

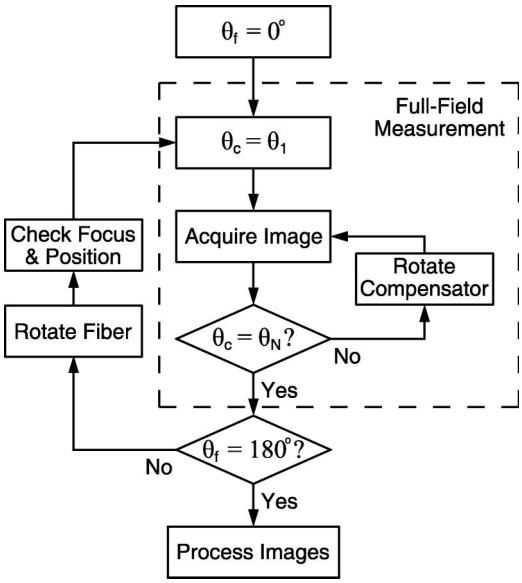

Fig. 3. Flow chart of the measurement process for determination of cross-sectional axial stress distributions. The dashed enclosed portion represents the image acquisition process for a full-field retardation measurement.

C. Tomographic Measurement

Determination of the full cross-sectional axial stress distribution requires retardation measurements spanning $0 \le \theta_f < 180°$. Measurements are made at various angles by rotating the fiber axially within the microscope. After the first full-field retardation measurement at $\theta_f = 0$, the fiber is rotated about its axis by a small amount. The focus and positioning of the fiber is checked, and occasionally radial runout requires the fiber to be recentered within the field of view and refocused. A full-field retardation measurement is then performed at the new rotation angle. The process of rotating the fiber and performing a full-field retardation measurement is repeated until the fiber has been rotated 180°. The entire flow chart in Fig. 3 represents the full procedure for obtaining the set of full-field retardation measurements necessary to determine the cross-sectional axial stress distribution. The fiber is rotated in increments of 2° for the results presented in this paper, which corresponds to 90 full-field retardation measurements.

D. Stress Calculation

To compute the cross-sectional axial stress distribution, only a single radial profile of the retardation is needed at each rotation angle of the fiber. A single radial profile of the retardation corresponds to a single column of pixels in a full-field retardation measurement. Thus, only a single column of pixels needs to be analyzed when determining the compensator angle producing minimum intensity as described previously. With a full set of radial retardation profiles, Eq. (6) is used to calculate the cross-sectional axial stress distribution. The ramp filter $|s|$ shown in Eq. (6) is multiplied by a Hann window. This enhances the accuracy of the reconstructed stress distribution in the fiber and smooths out edges and sharp transitions [31,32].

E. Experimental Apparatus

An Olympus BX60 microscope with polarization microscopy components enables full-field retardation measurements. A diagram of the relevant optical components is shown in Fig. 2. Illumination is provided by a mercury arc lamp and a 546 nm interference filter with a FWHM of 10 nm. Use of an incoherent light source eliminates interference effects due to diffraction of a coherent source, such as a He–Ne laser. A strain-free, polarizing condenser and strain-free 40× objective with a numerical aperture of 0.75 provide high-magnification imaging and minimize birefringence, which can induce background retardation. The polarizer and condenser are integrated into one housing, allowing for precise alignment of both optical components. The numerical aperture of the condenser is set to 80% of the objective to ensure high-quality Köhler illumination. Infinity-corrected objectives minimize wavefront distortion on the compensator, which immediately follows the objective. An Olympus U-CBR2 compensator with a retardation of 21.54 nm at the source wavelength of 546 nm is used for measurements performed on optical fibers. Digital images are captured using an Olympus Q-Color3 CCD. A cooled CCD and binning two-by-two blocks of pixels reduces noise in low-intensity images.

The optical fiber sample is rotated with a motorized rotation stage mounted next to the microscope. The fiber is held securely in the rotation stage with a fiber chuck and custom adapter to mount the chuck securely in the rotation stage. The fiber is held within the field of view of the microscope with a custom stage plate. Grooves in the custom plate allow for placement of fiber chucks on opposite sides of the field of view. Depressions in the plate allow for placement of a microscope coverslip and slide within the field of view. From the rotation stage, the fiber passes through one of the fiber chucks, between the coverslip and the slide, and through the second fiber chuck. The fiber chucks on the stage plate are not tightened on the fiber and serve to limit radial runout of the fiber as it is rotated. Index matching oil surrounds the fiber between the slide and the coverslip to minimize refraction from the cladding boundary. If there is excess fiber protruding from the second chuck on the stage plate, it is passed loosely through a fiber chuck next to the microscope to prevent bending that could impede rotation of the fiber.

Rotating the fiber in 2° increments over 180° requires 90 full-field measurements. Each full-field measurement requires incremental rotation of the compensator, typically 15–30 steps. To ensure repeatability in rotating the compensator, a custom coupling device enables automated rotation using another motorized rotation stage. The custom coupling device consists of two pieces. The first piece is a rubber-lined cup that securely fits onto the

rotation knob of the compensator. This piece features a square peg protruding in the direction of the rotation axis. This square peg fits into a square hole in the second piece, which mounts to the rotation stage. The square peg and square hole provide coupling but allow for slight misalignment between the rotation stage and the compensator. This ensures that no stress is imparted to the compensator housing.

4. Results

The presented stress profiling technique was used to assess two fiber modification processes where high retardation measurement accuracies were needed to characterize accurately the frozen-in stress present in the fiber. Stress modifications in Corning SMF-28 fiber due to (1) cleaving and (2) exposure to CO_2 laser radiation were investigated. To understand better the stress present after these modification processes, the stress present in an unperturbed Corning SMF-28 fiber was also characterized.

A. Unperturbed Fiber

The frozen-in axial stress distribution in an unperturbed Corning SMF-28 fiber is shown in Fig. 4. Positive values of axial stress indicate tensile stress and negative values indicate compressive stress. The distribution is azimuthally symmetric as expected. A relatively high tensile stress exists around the exterior of the cladding. The tensile stress decreases monotonically approaching the core of the fiber and becomes a compressive stress approximately 25 μm from the center of the fiber. Also visible is a ring of maximum compressive stress around the core of the fiber at the boundary between the core and cladding. This result agrees well with other published one-dimensional stress profiles [16,20,33] and two-dimensional stress distributions [23] in the same type of fiber.

The effects of both draw-induced (mechanical) stress and thermal stress are seen in the unperturbed fiber [3]. The presence of draw-induced stress is indicated by (1) the overall shape of the stress distribution and (2) the peak in compressive stress at the boundary between the core and cladding. The overall shape of the stress distribution is due to draw-induced (mechanical) stress effects. The tensile stress around the cladding of the fiber is due to the freezing-in of draw tension as the high-viscosity (thick) molten pure silica glass of the cladding solidifies. The low-viscosity (thin) molten glass in the core of the fiber, due to Ge doping, solidifies after the cladding and thus receives relatively small amounts of draw tension. When the drawing tension is removed from the fiber and mechanical equilibrium is established, the tensile stress in the cladding partially relaxes and imparts a compressive stress in and around the core of the fiber.

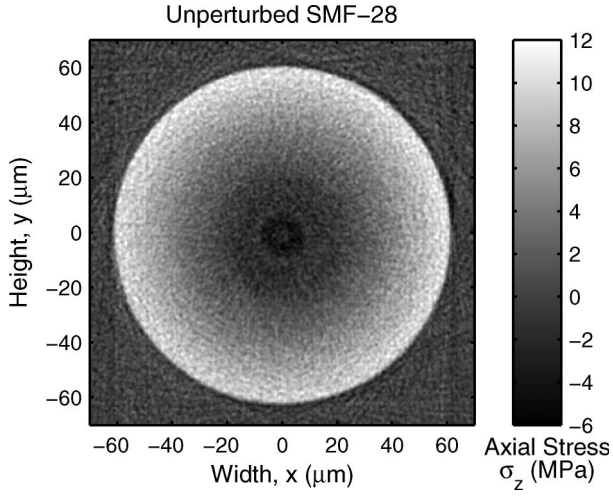

Fig. 4. Grayscale plot of a typical cross-sectional axial stress distribution in an unperturbed Corning SMF-28 fiber.

The peak in the compressive stress at the boundary between the core and cladding indicates the presence of OH impurities imparted during the manufacture of the fiber preform [34]. The OH impurities at the boundary significantly lower the viscosity of the molten silica glass. Therefore, similar to the core, the boundary region receives a relatively small amount of drawing tension. When the drawing tension is removed and mechanical equilibrium is established, a compressive stress is imparted in the boundary region.

The presence of thermally induced stress is indicated by the lower compressive stress in the core relative to the surrounding core–cladding boundary. The relatively high coefficient of thermal expansion in the Ge-doped core results in contraction of the glass as it cools. As the core contracts, tension is imparted to it as it conforms to the surrounding solidified cladding [3]. This thermally induced tensile stress counteracts the draw-induced compressive stress resulting in the lower compressive stress in the core relative to the surrounding core–cladding boundary.

Due to the azimuthal symmetry of the stress distribution, radial profiles at various angles can be averaged to reduce noise and further analyze the detailed features in the stress distribution. Radial profiles at azimuthal angles in 2° increments from 0 to 178° were averaged to produce an average axial stress profile. The average axial stress profile in the unperturbed fiber is shown with the solid line in Fig. 5. The effects of both draw-induced (mechanical) stress and thermal stress are seen clearly in the average profile. The peaks in the compressive stress at the boundary between the core and cladding are readily visible, as is the lower compressive stress in the core relative to the surrounding core–cladding boundary.

Observation of the cross-sectional stress distribution and average stress profile reveal a net tensile stress in the fiber. To analyze the origin of this net tensile stress, the mean axial stress in the fiber cross-section is evaluated. The mean axial stress is determined by

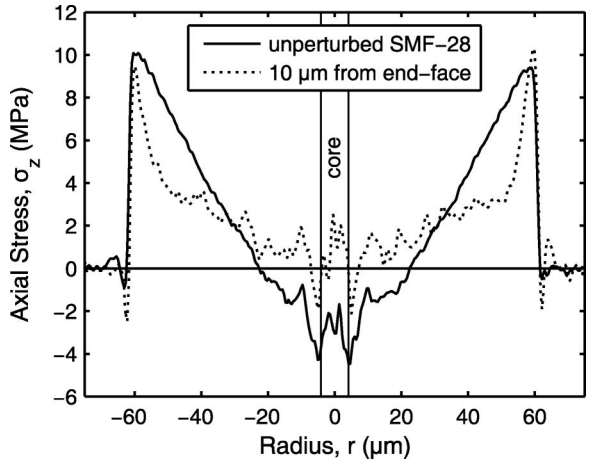

Fig. 5. Average radial profile of the stress distribution of the unperturbed Corning SMF-28 fiber (solid line) and the stress distribution 10 μm from the cleaved end-face (dotted line). Both profiles indicate peaks of compressive stress near the boundary between the core and cladding.

$$\bar{\sigma}_z = \frac{\int_0^{2\pi}\int_0^a \sigma_z(r,\theta) r \mathrm{d}r\mathrm{d}\theta}{\int_0^{2\pi}\int_0^a r\mathrm{d}r\mathrm{d}\theta}, \tag{8}$$

where a is the radius of the fiber cladding. The mean axial stress in the unperturbed Corning SMF-28 fiber is 4.71 MPa, indicating a mean axial tension in the fiber. However, in the absence of external forces, the mean stress in the fiber should be zero. The presence of an apparent nonzero mean stress is due to the photoelastic measurement technique from which the stress is calculated [33]. The measured retardation in the fiber is due to birefringence. The birefringence is then related to stress by the stress-optic law. However, the stress-optic law is only valid for stress-induced birefringence. The presence of structural anisotropy and its associated form birefringence also enters into the measured retardation, and thus, calculated stress. The apparent mean axial tension in the unperturbed fiber is due to measurement of not only the stress-induced birefringence, but also the form birefringence in the fiber. The origin of the form birefringence in the fiber is not known with certainty, but it has been hypothesized that inelastic strain is imparted to the fiber during manufacturing due to the viscoelasticity of the molten glass [3]. The time and temperature-dependent relaxation (viscoelasticity) of the molten glass during fiber manufacturing can cause the glass structure of the fiber to solidify anisotropically. This induced anisotropy, and thus form birefringence, is not due to frozen-in drawing forces and therefore exists along with stress-induced birefringence. This effect is often referred to as frozen-in viscoelasticity in the literature.

B. Fiber End-Face

The effect of cleaving the optical fiber was investigated by characterizing the frozen-in axial stress distribution near the cleaved end-face of a Corning SMF-28 fiber. The axial stress distribution 10 μm from the end-face of the fiber is shown in Fig. 6. For comparison to the axial stress distribution of the unperturbed fiber, the same maximum and minimum axial stress values are used to define the grayscale plot. Characterization of the stress distribution was degraded due to diffraction from the end-face, scattering from a particle on the end-face, and scattering from cleave imperfections. Despite the artifacts produced from this scattering, stress relaxation is apparent throughout the fiber cross section when compared to the unperturbed fiber.

Similar to the unperturbed fiber, the azimuthal symmetry of the stress distribution allows radial profiles at various angles to be averaged to reduce noise and analyze detailed features in the stress distribution. The average axial stress profile 10 μm from the end-face is shown with the dotted line in Fig. 5. In comparison to the average stress profile in the unperturbed fiber, there are two significant changes in the average stress profile near the end-face. First, with the exception of the outer edge of the cladding, relaxation of the tensile stress is seen in the outer cladding from a radius of 30 μm outward. The smaller tensile stress in the outer cladding of the cleaved fiber is consistent with partial relaxation of draw-induced tension. Second, inside 30 μm, the decreasing tensile stress and eventual increasing compressive stress in the unperturbed fiber appears as a consistent tensile stress in the cleaved fiber. The only significant compressive stress remaining near the cleaved end-face is at the boundary between the core and cladding, although the magnitude of the compressive stress is smaller than that in the unperturbed fiber. This shift to a tensile stress and lowering of compressive stress in and around the core of the cleaved fiber is consistent with relaxation of draw-induced stress. The draw-induced compression in and around the

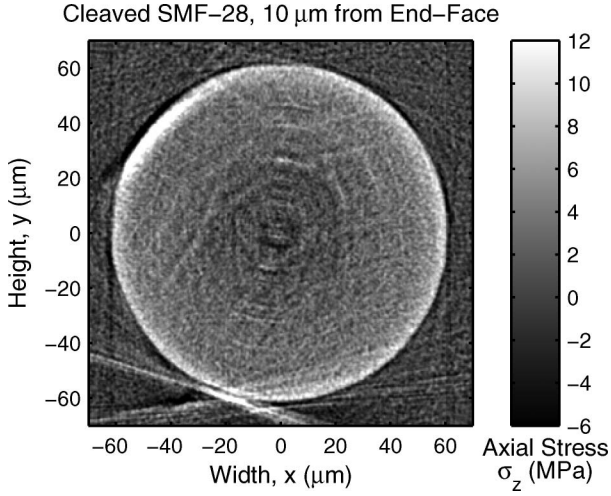

Fig. 6. Grayscale plot of the cross-sectional axial stress distribution 10 μm from the cleaved end-face of Corning SMF-28 fiber. For comparison to the unperturbed Corning SMF-28 fiber, the range of axial stress values shown is identical to that in Fig. 4. When compared to the unperturbed fiber, stress relaxation is evident throughout the fiber cross section.

core of the unperturbed fiber is relaxed, exposing the thermally induced tension in the Ge-doped core.

To investigate the presence of form birefringence, the mean axial stress inside the cleaved fiber was evaluated. The mean axial stress for various cross sections along the fiber axis is shown in Fig. 7. The mean axial stress was calculated using Eq. (8) as a function of distance from the cleaved end-face, z, where $z = 0$ is the end-face. Shown for comparison is the mean axial stress of 4.71 MPa in the unperturbed fiber. For distances greater than 40 μm from the end-face, no significant reduction in the mean axial stress is seen. However, from $z = 40\,\mu$m toward the end-face, the mean axial stress drops exponentially to a value of 1.12 MPa at $z = 0$. The decreased mean axial stress in the fiber near the end-face indicates a decrease in the form birefringence of the fiber. This indicates that fiber cleaving reduces the inelastic strain imparted to the fiber during manufacturing due to frozen-in viscoelasticity. However, the true extent of the relaxation of both frozen-in stress and frozen-in viscoelasticity is not known with certainty due to degradation of the retardation measurements within 5 μm of the end-face. Diffraction from the end-face and the presence of dust particles and cleave imperfections reduce the accuracy of the retardation measurements near the end-face and thus affect the calculated stress distributions.

C. Fiber Exposed to CO_2 Laser Radiation

The effect of exposing a fiber to CO_2 laser radiation was investigated by characterizing the frozen-in axial stress distribution in a single period of an LPFG fabricated in Corning SMF-28 fiber. The LPFG was fabricated by periodically exposing the fiber from one side to focused CO_2 laser radiation with a wavelength of 10.59 μm [8]. The characterized period of the LPFG was exposed for 220 ms with a laser power of 5.75 W and a focused beam diameter of 140 μm (373.5 W/mm^2). The axial stress distribution in the center of the region exposed to the laser radiation is shown in Fig. 8. The full range of axial stress values present in the fiber is shown in Fig. 8(a). The range of axial stress values is reduced in Fig. 8(b) to show the azimuthally asymmetric nature of the stress distribution. This azimuthal asymmetry is expected due to the one-sided exposure to the laser radiation. The dot–dashed center lines in Fig. 8 indicate the radial direction along which the asymmetry is strongest, and thus the direction of laser exposure. The radial profile of the axial stress along the direction of laser exposure is shown in Fig. 9. Also shown for comparison is a radial profile from the unperturbed fiber.

Significant changes are seen in the stress present in the exposed fiber when compared to the unperturbed fiber. The tensile stress around the cladding of the fiber becomes compressive after exposure to the CO_2 laser. Conversely, the compressive stress

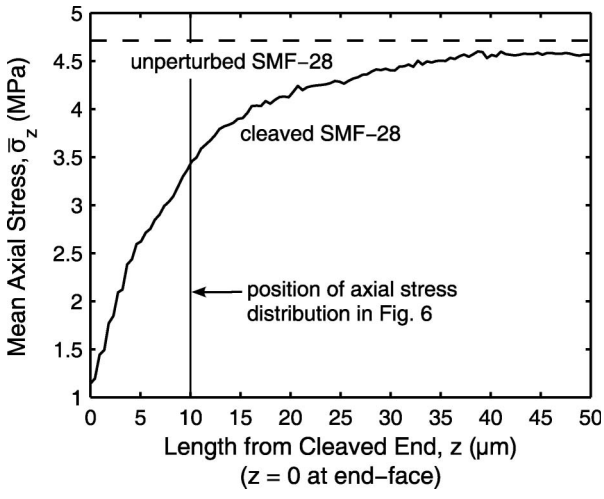

Fig. 7. Mean axial stress inside the fiber at various lengths from the cleaved end-face of the Corning SMF-28 fiber (solid curve). For comparison, the mean axial stress inside the unperturbed Corning SMF-28 fiber is shown (dashed line).

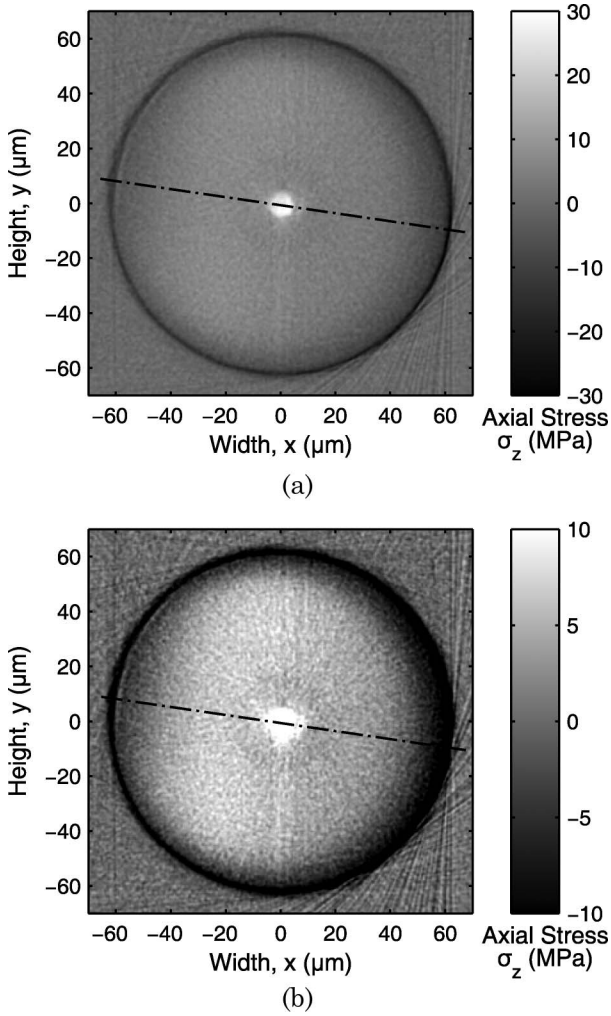

Fig. 8. Grayscale plots of the cross-sectional axial stress distribution at the center of a region of Corning SMF-28 fiber exposed to CO_2 laser radiation. The full range of axial stress values present in the fiber is shown in (a). The range of axial stress values is reduced in (b) to highlight the azimuthal asymmetry in the stress distribution. The dot-dashed center line indicates the radial direction along which the asymmetry is strongest.

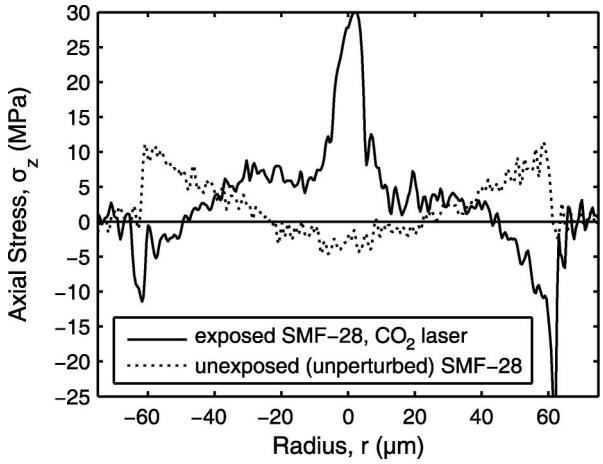

Fig. 9. Radial profile of the axial stress along the dot–dashed center line in Fig. 8(b) (solid line) and a typical radial profile of the axial stress in the unperturbed Corning SMF-28 fiber (dotted line).

in the core of the unperturbed fiber becomes strongly tensile in the exposed fiber. This change in the stress from laser exposure is consistent with draw-induced stress relaxation due to heating [9–11]. The draw-induced compression in and around the core of the unperturbed fiber is relaxed, exposing the thermally induced tension in the Ge-doped core. This effect is similar to the tension seen in the core near the cleaved end-face, however, the relaxation of the draw-induced compressive stress is more complete in the exposed fiber. Further evidence of draw-induced stress relaxation is the absence of the peak of compressive stress at the boundary between the core and cladding.

To investigate the presence of form birefringence, the mean axial stress inside the exposed fiber was evaluated. The mean axial stress for various cross sections along the fiber axis is shown in Fig. 10. The mean axial stress was calculated using Eq. (8) as a function of distance from the cleaved end-face, z. Shown for comparison is the mean axial stress of 4.71 MPa in the unperturbed fiber. The extent of the focused, 140 μm diameter beam on the fiber covers approximately $48 \le z \le 188\,\mu$m. Inside this region, the mean axial stress is less than 1 MPa. Outside of this region, the mean axial stress rapidly approaches the mean axial stress of the unperturbed fiber. The decreased mean axial stress in the exposed region indicates a decrease in the form birefringence of the fiber. This suggests that exposure to CO_2 laser radiation reduces the inelastic strain imparted to the fiber during manufacturing due to frozen-in viscoelasticity.

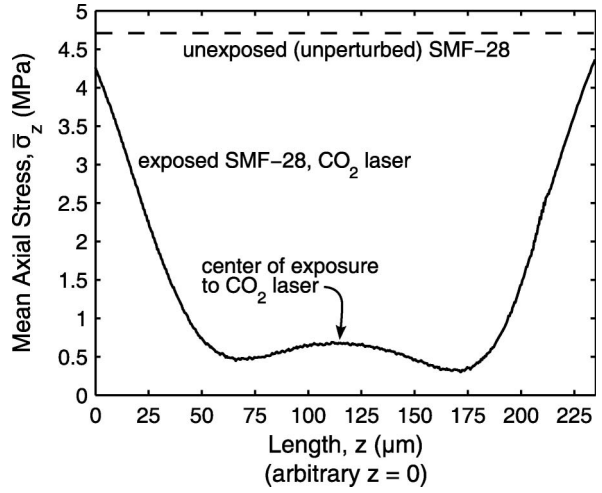

Fig. 10. Mean axial stress inside the fiber exposed to CO_2 laser radiation at various lengths along the fiber axis (solid curve). For comparison, the mean axial stress inside the unperturbed Corning SMF-28 fiber is shown (dashed line).

Also present in the exposed region is a slight increase in the mean axial stress at the center of exposure. It is hypothesized that this is due to the reintroduction of frozen-in viscoelasticity during exposure. The fiber is held under a small amount of tension during exposure with a 3.9 g mass attached to one end. The Gaussian shape of the CO_2 laser beam results in most of the laser power, and thus most of the heating occurring at the center of exposure. If the fiber is heated above the glass transition temperature, then conditions in the fiber in the center of exposure will be similar to those during drawing. When the exposure is finished and the fiber cools, a small amount of inelastic strain may be reintroduced, resulting in the slightly higher mean axial stress at the center of the exposure.

D. Assessment of Method

The performance of the presented cross-sectional stress profiling technique is assessed in terms of the spatial resolution and the background noise of the calculated axial stress. The spatial resolution was determined by analyzing the pixel spacing of the CCD camera used with the polarization microscope. The spatial resolution is 0.46 μm with the binning of two-by-two blocks of CCD pixels and the objective and condenser specifications listed in Subsection 3.E. This is slightly smaller than the lateral resolving power of the objective and condenser configuration of 0.49 μm, which results in oversampling the intensity for each two-by-two pixel block. However, this small amount of oversampling is permissible because the presented retardation measurement technique relies on detecting a minimum of intensity rather than absolute or relative intensities.

The background noise of the calculated axial stress was determined from the standard deviation of the background of the axial stress distribution in the unperturbed fiber. Calculating the noise in this manner accounts not only for the retardation measurement, but also for any effects from the image processing and filtered backprojection. The axial stress background noise for the presented technique is 0.69 MPa.

5. Summary

A cross-sectional profiling technique for the accurate characterization of the frozen-in stress in fibers and

fiber-based devices with small levels of birefringence has been developed. The Brace–Köhler compensation technique and a commercial polarization microscope yield high-accuracy full-field retardation measurements. From retardation measurements taken at multiple axial rotation angles of the fiber, computed tomography principles and filtered back-projection allow the determination of full cross-sectional axial stress distributions within the fiber. The profiling technique is determined to have a spatial resolution of $0.46\,\mu$m and a background noise of 0.69 MPa.

The profiling technique was used to characterize the axial stress distributions in Corning SMF-28 fiber in an unperturbed section, a section near a cleaved end-face, and a section exposed to CO_2 laser radiation. The effects of both draw-induced stress and thermal stress are seen in the unperturbed fiber. Furthermore, the presence of a mean axial stress of 4.71 MPa in the fiber indicates the presence of frozen-in viscoelasticity. Near the cleaved end-face, the axial stress distribution and average axial stress profile reveal greater amounts of thermally induced stress and relaxation of draw-induced stress. In addition, reduction in the mean axial stress in the fiber from 4.53 MPa at a distance of $40\,\mu$m from the end-face to 1.12 MPa at the end-face reveals relaxation of frozen-in viscoelasticity. In the region exposed to CO_2 laser radiation, the axial stress distribution reveals strong thermally induced stress indicating significant draw-induced stress relaxation due to heating. Mean axial stresses of less than 1 MPa in the exposed region also indicate the relaxation of frozen-in viscoelasticity. However, a slight increase in the mean axial stress at the center of exposure suggests the reintroduction of a small amount of frozen-in viscoelasticity.

References

1. G. W. Scherer, "Stress-induced index profile distortion in optical-waveguides," Appl. Opt. **19**, 2000–2006 (1980).
2. Y. Hibino, F. Hanawa, and M. Horiguchi, "Drawing-induced residual stress effects on optical characteristics in pure-silica-core single-mode fibers," J. Appl. Phys. **65**, 30–34 (1989).
3. A. D. Yablon, "Optical and mechanical effects of frozen-in stresses and strains in optical fibers," IEEE J. Sel. Top. Quantum Electron. **10**, 300–311 (2004).
4. D. I. Yeom, H. S. Kim, M. S. Kang, H. S. Park, and B. Y. Kim, "Narrow-bandwidth all-fiber acoustooptic tunable filter with low polarization-sensitivity," IEEE Photon. Technol. Lett. **17**, 2646–2648 (2005).
5. J. A. Buck, *Fundamentals of Optical Fibers* (Wiley, 2004).
6. I. H. Shin, B. H. Kim, S. P. Veetil, W. T. Han, and D. Y. Kim, "Residual stress relaxation in cleaved fibers," Opt. Commun. **281**, 75–79 (2008).
7. P. Y. Fonjallaz, H. G. Limberger, R. P. Salathe, F. Cochet, and B. Leuenberger, "Tension increase correlated to refractive-index change in fibers containing UV-written Bragg gratings," Opt. Lett. **20**, 1346–1348 (1995).
8. D. D. Davis, T. K. Gaylord, E. N. Glytsis, S. G. Kosinski, S. C. Mettler, and A. M. Vengsarkar, "Long-period fibre grating fabrication with focused CO_2 laser pulses," Electron. Lett. **34**, 302–303 (1998).
9. S. Yamasaki, M. Akiyama, K. Nishide, A. Wada, and R. Yamauchi, "Characteristics of long-period fiber grating utilizing periodic stress relaxation," IEICE Trans. Electron. **E83-C**, 440–443 (2000).
10. C.-S. Kim, Y. Han, B. H. Lee, W.-T. Han, U.-C. Paek, and Y. Chung, "Induction of the refractive index change in B-doped optical fibers through relaxation of the mechanical stress," Opt. Commun. **185**, 337–342 (2000).
11. B. H. Kim, Y. Park, T. J. Ahn, D. Y. Kim, B. H. Lee, Y. Chung, U. C. Paek, and W. T. Han, "Residual stress relaxation in the core of optical fiber by CO_2 laser irradiation," Opt. Lett. **26**, 1657–1659 (2001).
12. H. S. Ryu, Y. Park, S. T. Oh, Y. J. Chung, and D. Y. Kim, "Effect of asymmetric stress relaxation on the polarization-dependent transmission characteristics of a CO_2 laser-written long-period fiber grating," Opt. Lett. **28**, 155–157 (2003).
13. F. Durr, H. G. Limberger, R. P. Salathe, F. Hindle, M. Douay, E. Fertein, and C. Przygodzki, "Tomographic measurement of femtosecond-laser induced stress changes in optical fibers," Appl. Phys. Lett. **84**, 4983–4985 (2004).
14. F. Durr, G. Rego, P. V. S. Marques, S. L. Semjonov, E. M. Dianov, H. G. Limberger, and R. P. Salathe, "Tomographic stress profiling of arc-induced long-period fiber gratings," J. Lightwave Technol. **23**, 3947–3953 (2005).
15. P. L. Chu and T. Whitbread, "Measurement of stresses in optical fiber and preform," Appl. Opt. **21**, 4241–4245 (1982).
16. K. W. Raine, R. Feced, S. E. Kanellopoulos, and V. A. Handerek, "Measurement of axial stress at high spatial resolution in ultraviolet-exposed fibers," Appl. Opt. **38**, 1086–1095 (1999).
17. Y. Park, T.-J. Ahn, Y. H. Kim, W.-T. Han, U. C. Paek, and D. Y. Kim, "Measurement method for profiling the residual stress and the strain-optic coefficient of an optical fiber," Appl. Opt. **41**, 21–26 (2002).
18. Y. Park, S. Choi, U.-C. Paek, K. Oh, and D. Y. Kim, "Measurement method for profiling the residual stress of an optical fiber: detailed analysis of off-focusing and beam-deflection effects," Appl. Opt. **42**, 1182–1190 (2003).
19. L. Bruno, L. Pagnotta, and A. Poggialini, "A full-field method for measuring residual stresses in optical fiber," Opt. Lasers Eng. **44**, 577–588 (2006).
20. C. C. Montarou, T. K. Gaylord, and A. I. Dachevski, "Residual stress profiles in optical fibers determined by the two-waveplate-compensator method," Opt. Commun. **265**, 29–32 (2006).
21. T. Abe, Y. Mitsunaga, and H. Koga, "Photoelastic computer tomography: a novel measurement method for axial residual stress profile in optical fibres," J. Opt. Soc. Am. A **3**, 133–138 (1986).
22. Y. Park, U.-C. Paek, and D. Y. Kim, "Complete determination of the stress tensor of a polarization-maintaining fiber by photoelastic tomography," Opt. Lett. **27**, 1217–1219 (2002).
23. Y. Park, U.-C. Paek, and D. Y. Kim, "Determination of stress-induced intrinsic birefringence in a single-mode fiber by measurement of the two-dimensional stress profile," Opt. Lett. **27**, 1291–1293 (2002).
24. Y. Park, U.-C. Paek, and D. Y. Kim, "Characterization of a stress-applied polarization-maintaining (PM) fiber through photoelastic tomography," J. Lightwave Technol. **21**, 997–1004 (2003).
25. P. Kniazewski, T. Kozacki, and M. Kujawinska, "Inspection of axial stress and refractive index distribution in polarization-maintaining fiber with tomographic methods," Opt. Lasers Eng. **47**, 259–263 (2009).
26. T. Colomb, F. Durr, E. Cuche, P. Marquet, H. G. Limberger, R. P. Salathe, and C. Depeursinge, "Polarization microscopy by use of digital holography: application to optical-fiber birefringence measurements," Appl. Opt. **44**, 4461–4469 (2005).
27. B. Sevigny, F. Busque, N. Godbout, S. Lacroix, and M. Faucher, "High-resolution refractive index anisotropy measurement in

optical fibers through phase retardation modulation," Appl. Opt. **47**, 1215–1222 (2008).
28. C. C. Montarou and T. K. Gaylord, "Two-wave-plate compensator method for single-point retardation measurements," Appl. Opt. **43**, 6580–6595 (2004).
29. C. C. Montarou, T. K. Gaylord, B. L. Bachim, A. I. Dachevski, and A. Agarwal, "Two-wave-plate compensator method for full-field retardation measurements," Appl. Opt. **45**, 271–280 (2006).
30. H. Aben, *Photoelasticity of Glass* (Springer-Verlag, 1993).
31. J. Hsieh, *Computed Tomography: Principles, Design, Artifacts, and Recent Advances* (SPIE Press, 2003).
32. D. A. Viskoe and G. W. Donohoe, "Optimal computed tomography data acquisition techniques and filter selection for detection of small density variations," IEEE Trans. Instrum. Meas. **45**, 70–76 (1996).
33. Y. Park, U.-C. Paek, S. Han, B.-H. Kim, C.-S. Kim, and D. Y. Kim, "Inelastic frozen-in stress in optical fibers," Opt. Commun. **242**, 431–436 (2004).
34. B. H. Kim, Y. Park, D. Y. Kim, U. C. Paek, and W. T. Han, "Observation and analysis of residual stress development resulting from OH impurity in optical fibers," Opt. Lett. **27**, 806–808 (2002).